

Studies of Perovskite Materials for High Performance Piezoelectrics and Non-Volatile Memory

Tingting Qi, Joseph W. Bennett, Wissam Al-Saidi, Ilya Grinberg, and Andrew M. Rappe
The Makineni Theoretical Laboratories, Department of Chemistry, University of Pennsylvania,
Philadelphia, PA
 rappe@sas.upenn.edu

Abstract

Perovskite materials are crucial in a variety of important technological applications. Using quantum-mechanical simulations, we have computationally investigated ferroelectric materials for applications in computer memory and piezoelectric devices. We have determined that tetragonality of perovskite ferroelectrics, which is crucial for high piezoelectric performance, exhibits a quadratic dependence on the displacement of the B-site cations only. This provides guidance for the design of ferroelectrics and piezoelectrics with desired properties. We have also shown that a high piezoelectric response is likely to be present in lead-free, environmentally-friendly $\text{Sn}(\text{Al}_{1/2}\text{Nb}_{1/2}\text{O}_3)$ solid solutions. In a study of ultrathin ferroelectric films, we have shown that the details of metal-oxide bonding at the electrode-ferroelectric interface such as oxide termination play an important role in determining polarization stability and the miniaturization limit of ferroelectric devices.

1. Introduction

There is a need for perovskite oxides (formula ABO_3) with higher performance for use in a wide variety of applications such as actuators, sensors and data storage. For example, perovskite solid solutions with high piezoelectric response are used in current and next-generation military SONAR devices. When deformed by the external underwater sound vibrations, a piezoelectric material generates an electric field. This is then interpreted to gain information about depth, distance, and the identity of the source of the sound.

The flexible structure of perovskites lends itself to a variety of applications, depending upon the choice of *A*- and *B*-site atoms. In particular, the relationship between the sizes of the *A*-O and the *B*-O₂ sub-lattices plays an important role in determining the properties of the materials. This relationship is characterized by the tolerance factor (*t*) given by:

$$t = \frac{R_{\text{A-O}}}{R_{\text{B-O}}\sqrt{2}} \quad (1)$$

where $R_{\text{A-O}}$ is the sum of *A* and O ionic radii and $R_{\text{B-O}}$ is the sum of *B* and O ionic radii^[1]. Tolerance factor $t < 1$ usually leads to the rotation and expansion of the B-O₆ octahedra. Such octahedral rotations often generate a low-temperature anti-ferroelectric phase (e.g., PbZrO_3). If $t > 1$, the B-O₆ octahedra are stretched from their preferred B-O bond lengths, promoting B-cation distortions by creating room for the B-cations to move off-center. Therefore, simple perovskites with $t > 1$ are usually ferroelectric.

For example, when Pb and Ti are paired as *A* and *B*, respectively, these cations move in a concerted manner, so PbTiO_3 ($t = 1.06$) is ferroelectric. Ferroelectric ABO_3 oxides are sensors in SONAR devices and are also useful for non-volatile random access memory (NVRAM) devices. When external underwater sound vibrations deform such a SONAR device material, it generates an electric field which can then be interpreted to gain information about depth and distance and the identity of the source of the sound. Ferroelectric random access memory (FeRAM) is one of a growing number of alternative non-volatile memories, as it offers lower power usage, faster write-speed and a much greater maximum number of write-erase cycles.

Highly-accurate modeling is necessary to understand the origin of the various properties exhibited by perovskites used in the current state-of-the-art technology, in order to speed up the design of new materials with enhanced performance for

future devices. Over the last decade, first-principles calculations have emerged as a vital tool for understanding complex solid-state systems due to a combination of methodological improvements and faster computer speeds. In particular, density functional theory (DFT) is a powerful technique for the description of ground-state properties of metals, semiconductors, and insulators^[2,3] due to a combination of accuracy and computational efficiency. Here, we report on our first-principles DFT studies of materials design of new, lead-free piezoelectrics and relationships between composition and behavior of ferroelectric solid solutions.^[4,5] We also investigate polarization stability in ultra-thin ferroelectric films, important for miniaturization of non-volatile memory devices.^[6]

2. Results and Discussion

2.1 Correlations Between Tetragonality, Polarization, and Ionic Displacement in PbTiO₃-Derived Ferroelectric Perovskite Solid Solutions

The tetragonal lattice distortion plays a crucial role in the ferroelectric and piezoelectric properties of perovskites. For example, the best piezoelectric performance is found at the morphotropic phase boundary (MPB) of a solid solution between the tetragonal and the rhombohedral phases. Previous theoretical work has shown, that the strain-polarization coupling is vital for stabilizing the tetragonal phase relative to the rhombohedral one, and in enhancing the magnitude of polarization of the material.^[7] Recently, several Bi-based materials with extremely large polarization and c/a values were synthesized.^[8-10] These properties can be useful for applications such as birefringent optics and negative thermal expansion materials.^[11]

To enable rational materials design, it is necessary to understand how changes in a material's composition change the relevant properties. Previously, we demonstrated that there is a simple universal relationship between the ferroelectric-paraelectric transition temperatures in PbTO₃-based solid solutions and their 0K polarization (P^2), and elucidated how the crystal chemical changes due to compositional variations affect P and therefore T_c .^[12,13] Here, we study how crystal chemical properties of the material relate to its tetragonality.

Twenty-five different tetragonal ferroelectric materials were examined with DFT^[12,14] calculations and Berry's phase calculations^[15] to compute the polarization. The results of our calculations are presented in Table 1.

Table 1. DFT and experimental data for tetragonal PbTiO₃-derived ferroelectric perovskite solid solutions. A- and B-cation averaged displacements (D_A , D_B) and polarization (P), averaged over several different cation arrangements are obtained from DFT-relaxed structures. The $c/a-1$ and Curie temperature (T_c) data are from experimental literature^[8,16]. In the table, ABO₃ - (1-x) PT means x ABO₃ - (1-x) PT. The transition temperature datum for BiZn_{1/2}Ti_{1/2}O₃ is omitted, since this compound decomposed before undergoing phase transition^[9].

| | $c/a-1$ | P | T_c | D_B | D_A |
|---|---------|------|-------|-------|-------|
| PT | 0.065 | 0.87 | 765 | 0.280 | 0.450 |
| PbZn _{1/3} Nb _{2/3} O ₃ - 0.25 PT | 0.033 | 0.66 | 547 | 0.218 | 0.461 |
| PbZrO ₃ - 0.5 PT | 0.023 | 0.76 | 659 | 0.165 | 0.440 |
| PbSc _{1/2} Nb _{1/2} O ₃ - 0.5 PT | 0.020 | 0.50 | 560 | 0.142 | 0.296 |
| PbIn _{1/2} Nb _{1/2} O ₃ - 0.5 PT | 0.028 | 0.45 | 623 | 0.129 | 0.255 |
| PbSc _{2/3} W _{1/3} O ₃ - 0.625 PT | 0.020 | 0.61 | 517 | 0.176 | 0.350 |
| PbMg _{1/3} Nb _{2/3} O ₃ - 0.625 PT | 0.044 | 0.66 | 583 | 0.201 | 0.387 |
| PbZn _{1/3} Nb _{2/3} O ₃ - 0.625 PT | 0.048 | 0.74 | 643 | 0.241 | 0.424 |
| PbZrO ₃ - 0.67 PT | 0.046 | 0.84 | 700 | 0.210 | 0.450 |
| PbSc _{1/2} Nb _{1/2} O ₃ - 0.75 PT | 0.041 | 0.74 | 640 | 0.220 | 0.412 |
| PbIn _{1/2} Nb _{1/2} O ₃ - 0.75 PT | 0.046 | 0.65 | 695 | 0.208 | 0.387 |
| BiZn _{1/2} Ti _{1/2} O ₃ | 0.220 | 1.34 | | 0.489 | 0.903 |
| BiMg _{1/2} Ti _{1/2} O ₃ - 0.5 PT | 0.047 | 0.88 | 733 | 0.200 | 0.515 |
| BiZn _{1/2} Ti _{1/2} O ₃ - 0.5 PT | 0.120 | 1.17 | 1100 | 0.365 | 0.675 |
| BiMg _{1/2} Zr _{1/2} O ₃ - 0.75 PT | 0.041 | 0.86 | 721 | 0.216 | 0.478 |
| BiMg _{1/2} Ti _{1/2} O ₃ - 0.75 PT | 0.061 | 0.93 | 803 | 0.258 | 0.505 |

| | $c/a-1$ | P | T_c | D_B | D_A |
|--|---------|------|-------|-------|-------|
| BiZn _{1/2} Zr _{1/2} O ₃ - 0.75 PT | 0.064 | 0.93 | 740 | 0.263 | 0.508 |
| BiZn _{1/2} Ti _{1/2} O ₃ - 0.75 PT | 0.088 | 1.04 | 875 | 0.319 | 0.550 |
| BiScO ₃ - 0.75 PT | 0.040 | 0.84 | 768 | 0.220 | 0.488 |
| BiGaO ₃ - 0.75 PT | 0.057 | 0.84 | 768 | 0.226 | 0.447 |
| BiInO ₃ - 0.75 PT | 0.080 | 0.90 | 856 | 0.257 | 0.539 |
| BiAlO ₃ - 0.875 PT | 0.050 | 0.84 | 758 | 0.243 | 0.473 |
| BiScO ₃ - 0.875 PT | 0.053 | 0.85 | 780 | 0.257 | 0.442 |
| BiGaO ₃ - 0.875 PT | 0.057 | 0.83 | 757 | 0.241 | 0.427 |
| BiInO ₃ - 0.875 PT | 0.077 | 0.94 | 847 | 0.295 | 0.535 |

Inspection of the data in Table 1 shows that there is a general trend of higher c/a for materials with high P and large average A - and B -site off-center displacement magnitudes D_A^2 and D_B^2 as calculated from the ground-state structures obtained by our calculations. A closer examination of the correlation between tetragonality $c/a-1$ and P , D_A^2 , and D_B^2 shows that tetragonality is controlled by D_B . For example, for P and D_A there is a general trend of higher P or D_A values corresponding to higher $c/a-1$ (Figure 1), but with large deviations from the trend at high P values. On the other hand, for D_B the correlation with $c/a-1$ is strong and all of the data points fall close to the fit. The quality of the fit is not improved when D_A^2 , D_B^2 and the $D_A * D_B$ cross-terms are included; this proves that the dependence of $c/a-1$ on D_A is weak, and that the correlation between $c/a-1$ and D_A^2 is due to the coupling between the A - and B -site displacements.

The strong correlations observed in Figure 1 imply that for perovskite ferroelectrics there is a universal scaling of tetragonality with cation displacement and polarization. Tetragonality of different compositions can therefore be predicted from a modified Landau-Ginzburg-Devonshire (LGD) theory with the B -site displacement as the order parameter. The strain-displacement coupling contribution to the free energy can be described by:

$$G = -\gamma_A s D_A^2 - \gamma_B s D_B^2 - \gamma_{AB} s D_A D_B + \frac{1}{2} K s^2 \quad (2)$$

where s is the tetragonality $c/a-1$ and γ and K are the strain-displacement coupling and the elastic constants, respectively. Minimizing the free energy with respect to s , we get:

$$s = (\gamma_A D_A^2 + \gamma_B D_B^2 + \gamma_{AB} D_A D_B) / K. \quad (3)$$

The high quality of the fit to D_B data in Figure 1b means that γ_A and γ_{AB} are small compared to γ_B and can be neglected.

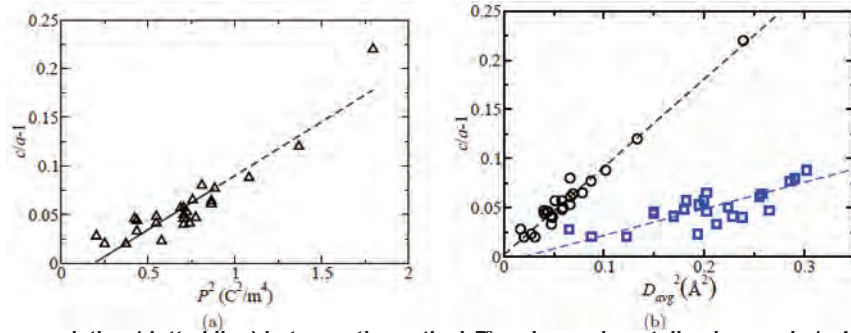


Figure 1. (a) A linear correlation (dotted line) between theoretical P^2 and experimentally observed $c/a-1$ is shown. (b) A linear correlation (dashed line) between the average cation displacement (D_A^2 in blue squares D_B^2 in black circles) and experimentally observed $c/a-1$ is shown. Better than D_A^2 and P^2 , D_B^2 most closely correlates with $c/a-1$.

On the other hand, for the standard form of the LGD theory of ferroelectrics where P_{tot} is the order parameter, the minimum-energy strain s is given by:

$$s = \gamma \left(Z_A^* D_A + Z_B^* D_B \right)^2 / K \quad (4)$$

where we rewrite P_{tot} as the sum of the A - and B -site contributions given by the average product of cation displacement and its Born effective charge Z^* .

This form enforces a scaling of the coupling between s and off-center displacements to be given by the ratio of the A - and B -site Born effective charges. However, from fit 3 in Table 2 it is clear that the γ_B/γ_A ratio is ≈ 13 , much larger than the ratio $(Z_B^*/Z_A^*)^2 = 3.4$ for PbTiO_3 . This disagreement is more severe for BZT $\left((Z_B^*/Z_A^*)^2 = 1.4 \right)$. It is the overestimation of the A -site contribution to the total strain-polarization coupling that weakens the correlation and makes P_{tot} a less-accurate predictor of c/a .

Table 2. R is the notation for correlation coefficient. D_B^2 exhibits the best linear correlation with s . Fitting parameters a , b , and d are in the unit of \AA^{-2} , e is in the unit of m^4C^{-2} , and c is unitless.

| Fitting functions | R |
|---|-------|
| $a * D_A^2 + c$ | 0.958 |
| $a = 0.2703, c = -0.0054$ | |
| $b * D_B^2 + c$ | 0.984 |
| $b = 0.8938, c = 0.0020$ | |
| $a * D_A^2 + b * D_B^2 + c$ | 0.985 |
| $a = 0.0553, b = 0.7236, c = -0.0003$ | |
| $d * D_A * D_B + c$ | 0.983 |
| $d = 0.5016, c = -0.0025$ | |
| $a * D_A^2 + b * D_B^2 + d * D_A * D_B + c$ | 0.985 |
| $a = 0.0000, b = 0.4796, d = 0.2346, c = -0.0003$ | |
| $e * P^2 + c$ | 0.924 |
| $e = 0.1108, c = -0.0208$ | |

The difference in the strain dependence on the A - and B -site displacements is due to the geometry of the perovskite unit cell. For the B -cations, the B -O bonds lie along the Cartesian axes. Therefore, an off-center displacement along a Cartesian direction strongly affects the B -O bonds along that direction. Increased strain along a Cartesian direction increases the lattice constant and creates more space for the B -cation distortion. This makes the B -cation off-centering displacement more energetically favorable^[7]. However, for the A -site, the A -O bonds lie along the (110) directions. Therefore, a tetragonal strain makes relatively small changes in the A -O bond length and strength. This makes the displacement-strain coupling for the A -cations weak.

Our understanding of how cation characteristics relate to the technologically important T_c and c/a properties of perovskite ferroelectrics provides a rational path for materials design. For example, since tetragonality scales with the B -site displacement, extreme tetragonality is not limited to Pb- or Bi-based materials but can be found even in compositions with a small charge on the A -site (e.g., Ag^{+1} -based ABO_3). For high T_c piezoelectric materials, an additive perovskite has to be chosen that will reduce c/a to create a morphotropic phase boundaries (MPB), while maintaining high T_c . To reduce c/a , the B -site displacement must be decreased. This; however, also tends to reduce T_c as it reduces the B -site contribution to polarization. Therefore, to keep T_c high, the A -site displacement must be increased by the additive perovskite. Such a combination of increased A -site displacement and decreased B -site displacement is in fact present for the two best high-temperature piezoelectric solid solutions available now – $\text{BiScO}_3\text{PbTiO}_3$ ^[17] and $\text{BiMg}_{1/2}\text{Ti}_{1/2}\text{O}_3 - \text{PbTiO}_3$ ^[16,18]. Upon addition of increasing amount of PbTiO_3 , these exhibit an immediate reduction of c/a accompanied by an initial rise in T_c . This leads to an enhancement of T_c^{MPB} compared to the classic $\text{Pb}(\text{Zr,Ti})\text{O}_3$ solid solution.

In conclusion, we have revealed a universal quadratic relationship between the average displacement of the cation B -site and c/a in ferroelectric perovskites. The composition-structure-property relations discovered in this and previous work provide guidance for systematic design of new ferroelectric and piezoelectric materials.

2.2 Pb-free Ferroelectrics Investigated with Density Functional Theory: Sn($\text{Al}_{1/2}\text{Nb}_{1/2}$) O_3 Perovskites

The search for more environmentally-friendly, lead-free piezoelectrics has led to the exploration of many new different perovskites with *A*-site ions such as Bi, Ag, and most recently, Sn. Investigations of Pb substitution by Sn are motivated by the chemical similarity between Pb^{2+} and Sn^{2+} cations. Both contain a stereochemically-active lone electron pair. Therefore, Sn atoms should exhibit large off-center displacements similar to the large Pb displacements in ferroelectric perovskites. Such displacements are favorable for a large polarization and a high ferroelectric-to-paraelectric transition temperature, T_c . The Sn analog of the classic PbTiO_3 material, SnTiO_3 has recently been studied with first-principles calculations and it was found that strong Sn off-centering is present, increasing both the c/a ratio and polarization relative to PT^[19]. Experimentally, synthesis of SnTiO_3 is difficult, due to the hypothesized small ionic size of Sn which decreases the tolerance factor below the optimal value, $t=1$, that predicts perovskite phase stability. It should be noted that the radius of Sn^{2+} in a 12-coordinate cage has not yet been tabulated. Another hindrance towards experimental synthesis is the possibility of either partial reduction or disproportionation of Sn at elevated temperatures. Therefore, stable Sn-based perovskites should be favored for *B*-site cations with a small ionic radius (to help increase t closer to 1) that tend to prevent reduction of Sn at high temperatures. We therefore choose $\text{Sn}(\text{Al}_{1/2}\text{Nb}_{1/2})\text{O}_3$ (SAN) for our investigation of Sn-based ferroelectrics, and use DFT calculations to study the properties of the SAN solid solution.

To study the impact of *B*-cation ordering on SAN properties, we perform calculations for all possible Sn/Nb arrangements in a 40-atom supercell. Of the 10 supercells studied, our calculations indicate that only 6 (supercells 1–6) are found to be unique; the remaining four (supercells 7–10) relax back to one of the unique set of supercells. The results of these calculations are presented in Table 3. We find that for the majority of supercells, the difference between lattice constants c and a are small (1.01–1.03), unlike the large c/a found for SnTiO_3 . All SAN supercells are ferroelectric with polarization magnitudes of 0.58–0.77 C/m² and a polarization vector close to either (110) or (111) directions.

Table 3. Data for the relaxed SAN supercells. Lattice constants, angles between axes and polarization values are given in Å, degrees and C/m², respectively. The energy differences relative to supercell 1 (ground state) are in eV per 40-atom supercell.

| Supercell | a | b | c | α | β | γ | Px | Py | Pz | Ptot | Ediff |
|-----------|-------|-------|-------|----------|---------|----------|------|------|------|------|-------|
| 1 | 7.789 | 7.887 | 7.887 | 89.5 | 90.0 | 90.0 | 0 | 0.43 | 0.43 | 0.61 | 0.000 |
| 2 | 7.938 | 7.933 | 7.777 | 90.0 | 90.0 | 89.5 | 0.54 | 0.54 | 0 | 0.77 | 0.039 |
| 3 | 7.806 | 8.033 | 7.825 | 89.3 | 90.0 | 90.0 | 0 | 0.52 | 0.34 | 0.62 | 0.699 |
| 4 | 7.831 | 7.942 | 7.858 | 89.5 | 90.0 | 90.0 | 0.0 | 0.46 | 0.41 | 0.62 | 0.408 |
| 5 | 7.887 | 7.874 | 7.868 | 90.1 | 90.2 | 89.7 | 0.44 | 0.28 | 0.25 | 0.58 | 0.406 |
| 6 | 7.917 | 7.784 | 7.918 | 90.0 | 90.5 | 90.0 | 0.53 | 0 | 0.52 | 0.74 | 0.067 |
| 7 | 7.938 | 7.777 | 7.933 | 90.0 | 89.5 | 90.0 | 0.54 | 0 | 0.54 | 0.77 | 0.039 |
| 8 | 7.806 | 7.825 | 8.033 | 89.3 | 90.0 | 90.0 | 0 | 0.34 | 0.52 | 0.62 | 0.699 |
| 9 | 7.831 | 7.858 | 7.941 | 89.5 | 90.0 | 90.0 | 0 | 0.41 | 0.46 | 0.62 | 0.408 |
| 10 | 7.869 | 7.875 | 7.887 | 89.8 | 90.2 | 90.1 | 0.25 | 0.28 | 0.44 | 0.58 | 0.406 |

For supercell 5, we find a triclinic ground-state structure. This is similar to the low-symmetry structures found at the MPB of $\text{Pb}(\text{Mg}_{1/3}\text{Nb}_{2/3})\text{O}_3\text{-PbTiO}_3$ (PMN-PT), PZT and other solid solutions. This low-symmetry is symptomatic of a flat potential energy surface, favorable for polarization rotation, which leads to a high electromechanical response at the MPB. Thus, our DFT results for supercell 5 indicate that pure SAN is close to the MPB, and a slight doping of a tetragonal additive will result in an MPB composition with good electromechanical properties.

High values of piezoelectric coefficients are an indication of proximity to the MPB; to prove our hypothesis, we therefore calculate the piezoelectric coefficients of SAN supercells. To obtain piezoelectric coefficients one needs to employ a response function calculation, which is computationally expensive for *each* 40-atom supercell. In the first step, displacements are made to the well-converged ground-state structure, for each atom, in each direction to generate a force constant matrix. Using this information, a series of mixed derivatives (second-derivative of total energy with respect to finite electric field, displacements, strain, etc.) are then used to obtain the response of the system in the framework of perturbation theory. In the case of piezoelectric coefficients, the mixed second-derivative of interest is total energy with respect to electric field and strain.

We find that for all supercells, the diagonal piezoelectric coefficients are larger than $e_{33}=2.7$ C/m² found for SnTiO₃ by Uratani, et al.^[19] and with the exception of supercells 1 and 4, are also larger than e_{33} coefficient of PbTiO₃. As expected, the similarity of supercell 5 to an MPB material leads to a particularly large $e_{33}=11.8$ C/m², essentially identical to the $e_{33}=12.6$ C/m² value of the monoclinic morphotropic phase boundary 50/50 PZT.^[20] The off-diagonal elements of the e tensor are mostly comparable to those found in PbTiO₃. However, for supercells 1 and 5 we find large values (10.5 C/m²) and e_{31} (7.3 C/m²) for some off-diagonal coefficients. The large piezoelectric coefficients for some of the SAN Al/Nb arrangements support our hypothesis that SAN is close to the MPB. All values for piezoelectric tensors can be found in the Supplemental material of Reference 5.

In order to predict the location of the MPB in the SAN solid solution, in which a tetragonal additive is added, such as adding PbTiO₃ to PbZrO₃ to create PZT, we use a previously developed theoretical model.^[21] If SAN is close to an MPB, then addition of tetragonal $ATiO_3$ would increase the electromechanical response. For a solid solution derived from PbTiO₃ (PT), the PT content at the MPB (x_{PT}^{MPB}) is given by:

$$x_{PT}^{MPB} = 1 - 1 / (0.34 + 3.31R_{B,avg} - 7.49D_{B,avg}^0), \quad (5)$$

where $R_{B,avg}$ is the average Shannon ionic radius for the B -site and $D_{B,avg}^0$ is the average reference ionic displacement of the B -site.

Due to the similar behavior of Pb and Sn on the perovskite A -site, we expect that Equation 5 will be valid for Sn-based ferroelectrics as well. Comparison of Al and Nb displacements in our relaxed SAN supercells shows that the Al displacements are 0.06 Å smaller on average than the Nb displacements. Therefore, we assign the reference Al displacement as 0.11 Å, 0.06 Å smaller than the 0.17 Å reference displacement for Nb. Substituting the D_B^0 values and the ionic radii (0.53 Å and 0.64 Å for Al and Nb, respectively) into Equation 5, we obtain $x_{PT}^{MPB} = 0.18$. Since the c/a ratio for SnTiO₃ is higher than that of PT, most likely less than 18% doping of SnTiO₃ will be needed to induce an MPB in a solid solution of SAN with SnTiO₃.

Local structure motifs in SAN are similar to those previously found for Pb-based perovskites.^[12] The polarization is caused by the concerted displacements of Sn, Al, and Nb cations from the center of their oxygen cages. Similar to PbTiO₃, the displacements of the A -site Sn atoms are much larger than those for the B -cations. The Sn displacements are sensitive to the local B -cation arrangement. For example, inspection of the Sn-Al and Sn-Nb partial-pair distribution functions (PDFs) obtained from supercell 3 (Figure 2) shows that the Sn-Al peaks are located at significantly shorter distances than the Sn-Nb peak. This is because the Sn atoms are off-center toward the underbonded O atoms with two Al neighbors, and away from the overbonded O atoms with two Nb neighbors.

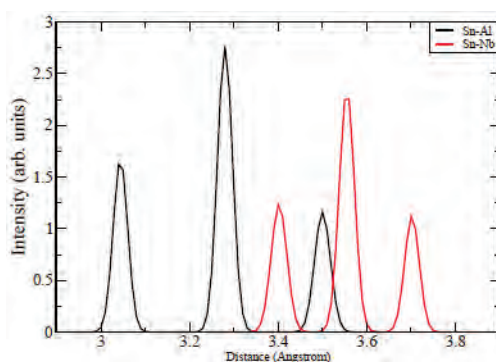


Figure 2. Sn- B -cation partial-pair distribution functions (PDF). Sn-Al and Sn-Nb partial PDFs are shown as solid black and dashed red lines respectively. On average, Sn-Nb distances are larger than Sn-Al distances, demonstrating that Sn displacements are directed away from Nb and toward Al.

To assign an ionic radius to the twelve-fold coordinated Sn²⁺ cation, we compare the Sn-O partial PDFs (Figure 3) with Pb-O and Bi-O partial PDFs from previous work^[11,22]. For all three PDFs, there are three sets of peaks indicating a presence of strong, medium and weak A -O bonds created by the A -cation displacements away from the center of the O₁₂ cage. Both the peaks for the strong and the weak Sn-O bonds are located at smaller distances than their Pb-O counterparts. This means that the ionic radius of 12-fold coordinated Sn²⁺ is smaller than that of 12-fold coordinate Pb²⁺ ($r_{Pb}=1.49$ Å). On the other hand, the Sn²⁺ ionic radius is larger than that of Bi³⁺ ($r_{Bi}=1.36$ Å). This is obvious from a comparison of the location of the

peak for the short Sn-O distances (2.3 Å) to the 2.1 Å location of the peak for the shortest Bi-O distances. The ionic size of Sn^{+2} is therefore ≈ 1.4 Å in the 12-fold coordination of the perovskite *A*-site, yielding $t=1.00$ for SAN solid solution and $t=0.99$ for SnTiO_3 .

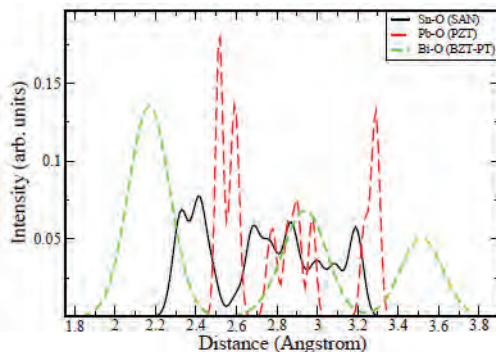


Figure 3. A comparison of Sn-O, Pb-O, and Bi-O partial PDFs. Sn-O shown in solid black line is obtained from current work, while Pb-O and Bi-O data from previous work^[11,22] are shown as dashed short (red) and long (green) lines respectively. Sn-O distances are smaller than those of Pb-O in PZT, but larger than the Bi-O distances in BZT-PT.

In conclusion, we have investigated the ground-state structure of the Pb-free ferroelectric material $\text{Sn}(\text{Al}_{1/2}\text{Nb}_{1/2})\text{O}_3$. We show that the electromechanical properties of SAN are similar to those found in ferroelectrics in close proximity to an MPB, which can be reached with by mixing SAN with a small amount of tetragonal additive. This is favorable for the development of Sn-based piezoelectrics to replace the Pb-based materials used in current devices.

2.3 Density Functional Study of PbTiO_3 Nanocapacitors with Pt and Au Electrodes

Ferroelectric (FE) nano-capacitors have been under intense investigation in the last decade due to their potential use for nonvolatile (FE) random-access memory (FERAM) devices.^[23–25] A crucial issue for FERAM miniaturization is the critical thickness at which ferroelectricity and polarization can no longer be sustained due to the presence of a strong depolarizing field. We investigate nano-capacitors consisting of PbTiO_3 ferroelectric with Pt and Au electrodes to gain a thorough understanding of the electrode-FE interfaces, and to elucidate the role of the interfacial chemical bonding and charge transfer in stabilizing the FE polar phase.

We use DFT calculations with the recently developed PBEsol functional^[26] to study properties of several PTO-based nano-capacitor-like structures. As shown by Perdew and collaborators^[27], PBEsol is more accurate for solids and surfaces, while the well-known PBE functional^[27] gives better results for atoms and molecules.

To represent the capacitors, we used a supercell containing an alternating stack of PbO and TiO_2 layers sandwiched between metal electrodes. We study both TiO_2 and PbO terminations of PbTiO_3 and FE thicknesses of $n=1\dots 11$ unit cells. For the TiO_2 termination, the metal atoms are located on top of the oxygen atoms and for the PbO termination they are on top of the *A*-cation and oxygen atoms.

The results for the nano-capacitors at the critical thickness are presented in Table 4. We find that the critical thickness is 24 Å for TiO_2 termination. We also present the data for PbO termination and 28 Å for interfacial polarization at the positive and negative surfaces, and the average polarization of the FE thin films. Our results show that the critical thickness of ferroelectricity is not only a function of composition of the oxide and metal, but also of the termination of the oxide film (TiO_2 vs. PbO). The FE-electrode interfaces are significantly different for the two terminations. For example, for Pt electrodes, the layer polarization magnitudes at the positive and negative surfaces are much smaller for the TiO_2 termination than for the PbO termination. Similarly, for the TiO_2 termination, Pt electrodes stabilize a larger fraction of bulk *P* than the Au electrodes. This is in contrast to the PbO termination for which our calculations find Au electrodes to be better.

Table 4. Computed properties of PTO-based nano-capacitors with different electrodes. N_c is the smallest number of unit cells for which the film has a FE ground state. The layer polarization at the negative (P_-) and positive (P_+) interfaces, and the average polarization (P_{av}) of the FE film, are all in units of the bulk polarization P_{bulk} . The layer polarization, given in units of the bulk polarization, is defined as the ratio of the rumplings of the cations from their oxygen cages in the thin film to those in the bulk. c/c_{bulk} measures the tetragonality of the FE film in units of the bulk value, and Δ (meV) is the well depth of the FE film per surface unit cell.

| | N_c | P_-/P_{bulk} | P_+/P_{bulk} | P_{av}/P_{bulk} | c/c_{bulk} | Δ |
|------------------------|-------|----------------|----------------|-------------------|--------------|----------|
| TiO ₂ term. | | | | | | |
| Pt/PTO/Pt | 7 | 0.50 | 0.62 | 0.62 | 0.94 | 7 |
| Au/PTO/Au | 7 | 0.77 | 0.86 | 0.80 | 0.96 | 16 |
| PbO term. | | | | | | |
| Pt/PTO/Pt | 6 | 0.99 | 0.97 | 0.95 | 0.96 | 45 |
| Au/PTO/Au | 6 | 0.44 | 0.38 | 0.35 | 0.96 | 31 |

We use average polarization P of the nano-capacitors shown in Table 4 to estimate the effective screening length λ of the metallic electrodes. The depolarizing field is given by:

$$E_d = -\frac{2\lambda P}{\epsilon_0 \ell}, \quad (6)$$

where ℓ is the thickness of the FE film^[28]. We obtain E_d by macroscopic-averaging^[29] of the electrostatic potential. We find $\lambda=0.045$ and 0.028 Å for Pt and Au with TiO₂ termination, and 0.007 and 0.034 Å with PbO termination, respectively. These effective screening lengths are not intrinsic properties of the electrode, but of the electrode-oxide interface, and are much smaller than the standard screening lengths of metals (≈ 0.5 Å for Pt and ≈ 0.8 Å for Au).

Analysis of structural data shows that the deformations from the parent oxide and metal geometry are localized at the metal-oxide interface. For the oxide, the layer polarization for the 1–2 layers close to the interfaces is either enhanced or diminished compared to the polarization in the layers far from the electrode (Figure 4). Similar effect is seen in the buckling of the electrode layers (Table 5) for the PbO terminations. For the TiO₂ termination there is no buckling in the electrode layers because the metal atoms are in a symmetric chemical environment. The magnitude of the buckling for the Pt and Au electrodes is correlated with the strength of the metal-oxide bonds at the interface. These are stronger for Pt-O (bond enthalpy of 347 kJ/mole) than for Au-O (bond enthalpy of 222 kJ/mol).

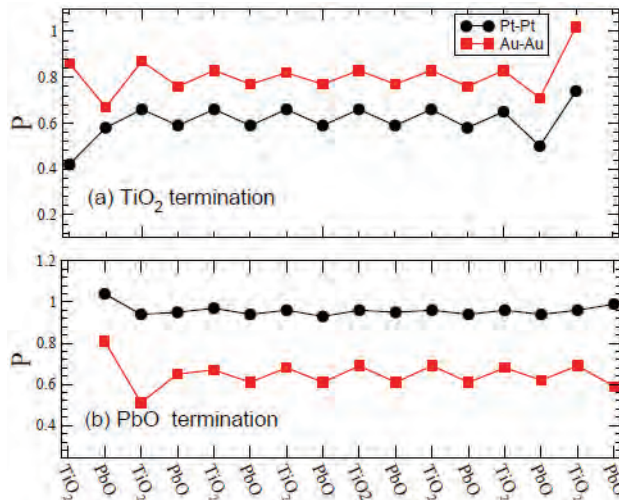


Figure 4. The layer polarization profile for the TiO₂ and PbO nano-capacitors with Pt and Au electrodes. We measure the polarization with respect to the bulk polarization of PTO. All films have seven unit cells.

Table 5. Buckling (in Å) of the electrode layers that are in registry with the PbO layers. We report these values for the PE nano-capacitors (β_0), and for the negative (β_-) and positive (β_+) surfaces of the FE nano-capacitors.

| | PbO termination | | | TiO ₂ termination | | |
|------|-----------------|-----------|-----------|------------------------------|-----------|-----------|
| | β_0 | β_- | β_+ | β_0 | β_- | β_+ |
| PtPt | | | | | | |
| 1st | -0.347 | -0.314 | -0.023 | 0.012 | 0.007 | 0.017 |
| 2nd | 0.019 | 0.013 | 0.021 | -0.005 | 0.008 | -0.015 |
| 3rd | 0.000 | -0.011 | | | | |
| AuAu | | | | | | |
| 1st | -0.195 | -0.247 | 0.074 | -0.062 | -0.015 | 0.068 |
| 2nd | -0.041 | -0.064 | 0.006 | -0.013 | -0.008 | -0.005 |
| 3rd | -0.000 | -0.043 | | | | |

Our results show that the chemical bonding at the interface significantly changes the electronic surface of the interface oxide layers. Figure 5 shows layer-projected density-of-states (LPDOS) for the TiO₂- and PbO-terminated FE nano-capacitors with Pt and Au electrodes. In these films, the polarization is directed upwards, i.e., the lower interfacial layer is at the negative surface and the upper one is at the positive surface. Examination of the LPDOS shows two main effects of the metal-oxide bonding. First, the interfacial oxide layers are metallic with a large density-of-states at the Fermi level. This is due to the charge transfer taking place at the interface, and is also the case for the paraelectric structure. Second, for the ferroelectric films, the conduction band on the positive surface is shifted downward and the valence band at the negative surface is shifted upwards. Similar to the structural changes, these effects are localized at the interface as can be seen from the LPDOS of the oxide layers in the bulk of the film which are similar to those of bulk PTO.

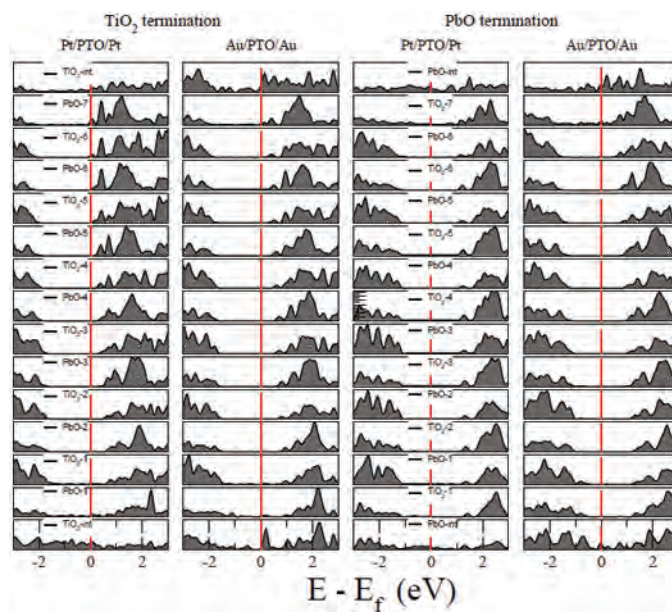


Figure 5. The layer-projected density of states for the TiO₂ and PbO terminated FE nano-capacitors with Pt and Au electrodes. The polarization is directed upwards i.e., the lower TiO₂ interfacial layer is at the negative surface of the capacitor and the upper one is at the positive surface. All the nano-capacitors have 15 oxide layers (seven unit cells).

In conclusion, we presented an *ab initio* investigation of ferroelectricity in single-domain PbTiO₃ (PTO) based nano-capacitors. The ferroelectric properties of the thin films depend on the details of the electrodeperovskite interface, with difference in screening properties between the TiO₂ and PbO terminations of the oxide. The critical thickness is 24–28 Å.

3. Significance to DoD

Perovskite oxides form the basis for a range of military-relevant technologies such as dielectric ceramics for capacitor applications, ferroelectric thin-film non-volatile memories, piezoelectric materials for SONAR and actuators, and electro-optic materials for data storage and displays. A microscopic understanding of perovskite oxides properties is critical for the goal of designing new materials. Once the relationships between the atomic composition, structure and materials properties are understood, new materials that improve upon existing technology can be designed. The US Navy would reap a considerable military advantage from more robust ferroelectric memory impervious to electromagnetic pulse attacks, higher-performance SONAR for detection of submarines, and photovoltaic materials for energy generation. Our investigations of composition-structure-property relationships in perovskite ferroelectrics provide a rational path for design of new piezoelectric SONAR materials with enhanced sensitivity and robustness. Our study of lead-free tin-based piezoelectrics shows that this class of materials is likely to exhibit high piezoelectric performance similar to that of the current lead-based perovskites. Our examination of ferroelectric nano-capacitors shows the importance of the oxide termination for the behavior of the metal-oxide interface that controls polarization stability and sets the limit to the miniaturization of nonvolatile memories and other ferroelectric-based devices.

Computational Technology Area

Computational Material Science

Acknowledgements

This work was supported by the Office of Naval Research under grants N00014-09-1-0157 and N00014-09-1-0455, by the Air Force Office of Scientific Research Grant No. FA9550-10-1-0248, the MEREST grant, and the DMR05-20020. This work was also supported by the US Department of Energy Office of Basic Energy Sciences, under grant number DE-FG0207ER15920 and DE-FG02-07ER46431. Computational support was provided by a Challenge grant from the High Performance Computing Modernization Program of the US Department of Defense.

References

1. Goldschmidt, V.M., *Die Naturwissenschaften*, 21, 477, 1926.
2. Hohenberg, P. and W. Kohn, *Phys. Rev.*, 136, B864, 1964.
3. Kohn, W. and L.J. Sham, *Phys. Rev.*, 140, A1133, 1965.
4. Bennett, J.W., I. Grinberg, P.K. Davies, and A.M. Rappe, *Phys. Rev. B*, 83, 144112, 2011.
5. Qi, T., I. Grinberg, and A.M. Rappe, *Phys. Rev. B*, 82, 134113, 2010.
6. Al-Saii, W.A. and A.M. Rappe, *Phys. Rev. B*, 82, 155304, 2010.
7. Cohen, R.E., *Nature*, 358, 136, 1992.
8. Suchomel, M.R. and P.K. Davies, *Appl. Phys. Lett.*, 86, 262905, 2005.
9. Suchomel, M.R. A.M. Fogg, M. Allix, H. Niu, J.B. Claridge, and M.J. Rosseinsky, *Chem. Mater.*, 18, 4987, 2006.
10. Stein, D.M., M.R. Suchomel, and P.K. Davies, *Appl. Phys. Lett.*, 89, 132907, 2006.
11. Grinberg, I., M.R. Suchomel, W. Dmowski, S.E. Mason, H. Wu, P.K. Davies, and A.M. Rappe, *Phys. Rev. Lett.*, 98, 107601, 2007.
12. Grinberg, I. and A.M. Rappe, *Phys. Rev. B*, 70, 220101, ISSN 0163-1829, URL <http://dx.doi.org/10.1103/PhysRevB.70.220101>, 2004.
13. Grinberg, I. and A.M. Rappe, *Phys. Rev. Lett.*, 98, 037603, 2007.
14. Perdew, J.P. and A. Zunger, *Phys. Rev. B*, 23, 5048, 1981.
15. Vanderbilt, D. and R.D. King-Smith, *Phys. Rev. B*, 48, 4442, 1993.
16. Suchomel, M.R. and P.K. Davies, *J. Appl. Phys.*, 96, 4405, 2004.
17. Eitel, R.E., S.J. Zhang, T.R. Shrout, C.A. Randall, and I. Levin, *J. Appl. Phys.*, 96, 2828, 2004.
18. Randall, C.A., R. Eitel, B. Jones, T.R. Shrout, D.I. Woodward, and I.M. Reaney, *J. Appl. Phys.*, 95, 3633, 2004.
19. Uratani, Y., T. Shishidou, and T. Oguchi, *Jap. J. Appl. Phys.*, 47, 7735, 2008.
20. Wu, Z. and H. Krakauer, *Phys. Rev. B*, 68, 014112, 2003.
21. Grinberg, I., M.R. Suchomel, P.K. Davies, and A.M. Rappe, *J. Appl. Phys.*, 98, 094111, 2005.

22. Grinberg, I., V.R. Cooper, and A.M. Rappe, *Phys. Rev. B*, 69, 144118, 2004.
23. Junquera, J. and P. Ghosez, *Nature*, 422, 506, 2003.
24. Sai, N., A.M. Kolpak, and A.M. Rappe, *Phys. Rev. B Rapid Comm.*, 72, 020101, R, 2005.
25. Stengel, M., D. Vanderbilt, and N. Spaldin, *Nat. Mater.*, 8, 392, 2009.
26. Perdew, J., A. Ruzsinszky, C. G^ábor, O. Vydrov, G. Scuseria, L. Constantin, X. Zhou, and K. Burke, *Phys. Rev. Lett.*, 100, 136406, 2008.
27. Perdew, J.P., K. Burke, and M. Ernzerhof, *Phys. Rev. Lett.*, 77, 3865, 1996.
28. Mehta, R.R., B.D. Silverman, and J.T. Jacobs, *J. Appl. Phys.*, 44, 3379, 1973.
29. Baldereschi, A., S. Baroni, and R. Resta, *Phys. Rev. Lett.*, 61, 734, 1988.